Supporting Information

Heterostructures of Vertical, Aligned and Dense SnO_2 Nanorods on Graphene Sheets: in-situ TEM Measured Mechanical, Electrical and Field Emission Properties

Zou Rujia,[a] Zhenyu Zhang,[a] Kaibing Xu,[a] Lin Jiang,[a] Qiwei Tian,[a] Shaolin Xue,[a] Junqing Hu,[a*] Yoshio Bando[b] and Dmitri Golberg[b]

[a] State Key Laboratory for Modification of Chemical Fibers and Polymer Materials, College of Materials Science and Engineering, Donghua University, Shanghai 201620, China

[b] International Center for Materials Nanoarchitectonics (MANA), National Institute for Materials Science (NIMS), 1-1 Namiki, Tsukuba, Ibaraki 305-0044, Japan,

*Corresponding authors. E-mail: hu.junqing@dhu.edu.cn

I . The reduced graphene sheets' preparation

0.01 g of graphite oxide sheets were ultrasonically dispersed into 10 mL of absolute ethanol in a capped bottle, followed by ultrasonic stirring for 1 h to form a homogeneous suspension. The homogeneous suspension was spin-coated on a SiO_2/Si substrate at 1000 rpm over 2 min, and then thermally reduced at 650 °C for 30 min under a 100 sccm H_2 gas flow. Figs. S1a and b reveal that the as-grown reduced graphene sheets (rGss) are multi-layered ($\leq$ 8 nm) with a mean area of ~ 10-300 μm^2. The Raman spectrum was dominated by two intensive peaks at 1331 and 1578 cm^{-1}, which are referred as D line and G line (Fig. 1c), respectively. The G line corresponds to the tangential stretching (E^2_{2g}) mode of highly oriented pyrolytic graphite (HOPG), indicating the presence of crystalline graphite; the D line is originated from a resonant coupling of the excitation laser with electronic states associated with disordered graphite materials. The Raman spectra measured from graphene sheets show a strongly G-band peak, which slao indicating that the as-grown graphene sheets are multi-layered.

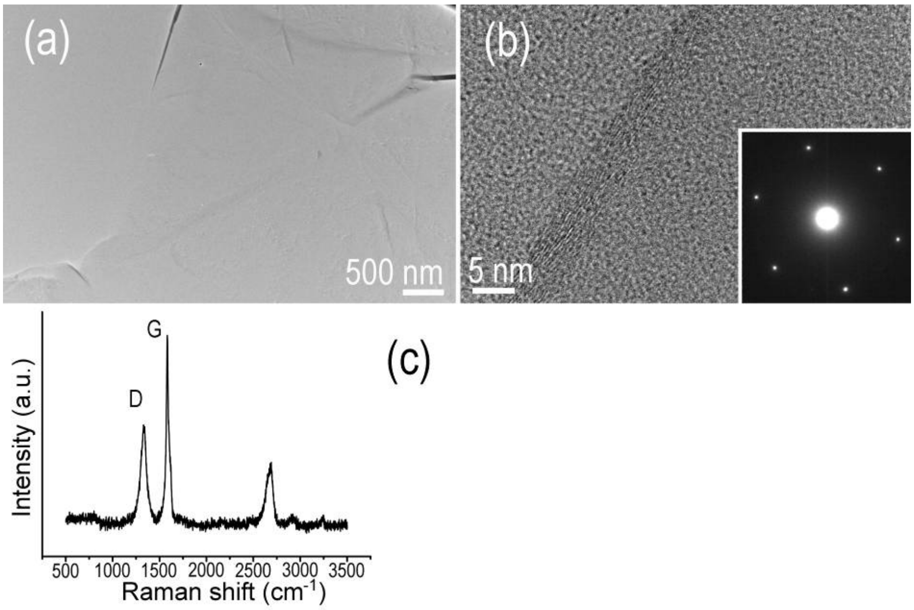

Fig. S1 (a) TEM image shows a rGs. (b) High-resolution TEM image displays that the rGs is multi-layered; the inset shows its electron diffraction pattern. (c) Raman spectroscopy of the graphene sheets.

II. Growth of SnO_2 nanorod arrays on a single side of free-standing rGss

The synthetic procedure is schematically described in Fig. S2. An organic paste was mixed with ethyl cellulose (5%) and terpineol upon sufficient stirring in an agate bowl to make the homogeneous paste which was then spin-coated on a glass substrate at 2000 rpm over 2 min. The as-coated glass substrate with a thin layer of the organic paste was dried at 100 °C in air for 45 min (Figs. S2a and b). A dispersion of 0.01 g rGss was prepared by ultrasonic dispersion in alcohol for 2 h, that was spin-coated on the paste-coated glass substrates at 1000 rpm over 2 min. After annealling at 150 °C for 30 min under a N_2 flow, the rGss were firmly coated on the glass substrates (Fig. S2c). Then, the rGss coated substrates were plunged in a $SnCl_4 \cdot 5H_2O$ solution (0.005 M of $SnCl_4 \cdot 5H_2O$ in 20 mL deionized water) for 2 h, and then a layer of SnO_2 nanocrystals (due to hydrolysis at room temperature) was seeded on the surface (a single side) of the rGss (Fig. S2d). After that, the substrate was taken out of the $SnCl_4 \cdot 5H_2O$ solution and then heated to 350 °C in air for 2 h in order to remove the organic paste and to further improve the crystallinity of SnO_2 nanocrystal seeds on the rGss' surface (Fig. S2e). The SnO_2 nanocrystal-seeded rGss were stripped from the glass substrate (Fig. S2f), and then mixed with $SnCl_4 \cdot 5H_2O$ (0.025 M), NaOH (0.75 M), $C_{12}H_{25}NaO_4S$ (0.125 M), and 50 mL deionized water. After ultrasonic dispersion, the homogeneous microemulsion formed; that was transferred into a 60 mL autoclave and heated at 220 °C for 14 h. The obtained product was washed several times with ethanol and distilled water, successively, and dried in vacuum at 60 °C for 12 h. As a result, the SnO_2 nanorods emerged as densely packed filaments perpendicular to the surface of the rGss to form two-layered heterostructures of SnO_2 nanorod arrays and free-standing rGss, as shown in Fig. S2g. It can be transferred to desired substrate in order to design rGs-based devices with special requirement (Fig. S2h).

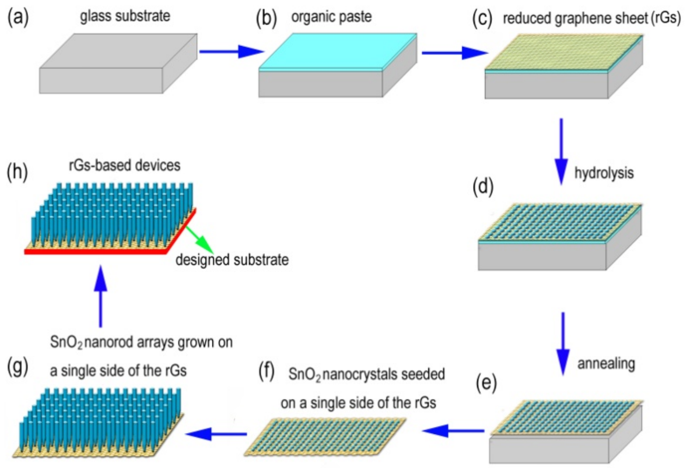

Fig. S2 Schematic illustratration of the consecutive processes of the SnO_2 nanorod arrays growth on a single side of the rGs forming two-layered heterostructures of SnO_2/rGs via the NSDH route:

(a) a glass substrate, (b) organic paste spin-coated on the glass substrate, (c) rGs spin-coated on the paste-coated glass substrate, (d) hydrolysis process, (e) annealing process, (f) SnO_2 nanocrystal-seeded rGs stripped from the glass substrate, (g) SnO_2 nanorod arrays are grown on the single side of the free-standing rGs via a hydrothermal process, and (h) designment of the rGs-based device on desired substrate.

Figure S3 schematically illustrates the nucleation and growth of SnO_2 nanorod arrays on a single side of free-standing rGss via the NSDH route. First, the uniform and dense SnO_2 nanocrystals were seeded over a single side of the rGss due to the hydrolysis of the reaction precursors, as shown by the two upper images in Fig. S3a. TEM image in Fig. S3b shows the SnO_2 nanocrystals seeded on a single side of the rGss during hydrolysis. Second, upon the hydrothermal process within the solution (consisting of the SnO_2 nanocrystal seeded rGss and the reaction precursors), the nucleation of SnO_2 nanorods took place, which was activated and directed by the SnO_2 nanocrystal seeds on the rGss. The initial growth of the nanorods started on these nanocrystal seeds along their preferential orientations with a low energy plane, resulting in their placement at the tips or attachment to the ends of SnO_2 nanorods, as suggested by a high-resolution TEM (HRTEM) image, Fig. S3c. Finally, highly dense SnO_2 nanocrystal seeds on the rGss led to the concurrent growth of a large number of the SnO_2 nanorods over the graphene sheets. The overcrowding effect confined the propagation of the SnO_2 nanorods predominantly in the vertical direction, except for those formed at the exposed edges where the SnO_2 nanorods could grow freely.[1,2] So, the SnO_2 nanorods emerged as dense alignments perpendicular to the surface of the rGss to form two-layered heterostructures of SnO_2 nanorod arrays and free-standing rGss, as shown by the bottom image in Fig. S3a.

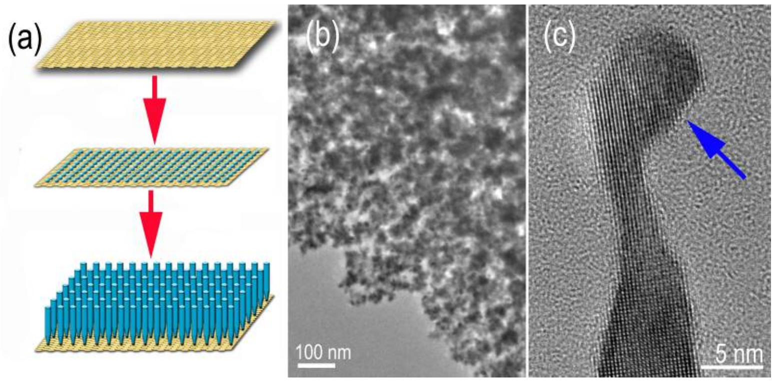

Fig. S3 (a) Schematics illustrate the processes of the SnO_2 nanorod arrays growth on a single side of the free-standing rGs to form two-layered heterostructures of SnO_2/rGs via the NSDH route. (b) TEM image shows the SnO_2 nanocrystals seeded on a single side of the rGs through the hydrolysis of the reaction precursors. (c) A HRTEM image displays a SnO_2 nanocrystal seed tipped a SnO_2 nanorod.

Figure 4 shows the typical FTIR spectra of SnO_2 nanorods on reduced graphene sheets (SnO_2/rGss), which the intensities of modes from oxygen functionalities were significantly reduced compared with the intensities of graphene oxide. [3-6] The sample of SnO_2/rGss has two strong peaks at 3430 cm^{-1} (O-H stretching vibrations) and 1633 cm^{-1} (skeletal vibrations from graphitic domains) due to the adsorbed water and aromatic C=C. The FTIR spectra was also dominated by two peaks at 1400 and 1058 cm^{-1}, which are referred as vibrations from C-O groups situate on the rGss. In comparison to the FTIR spectrum of GO,[3-6] the peaks at 1723 cm^{-1} (C=O stretching vibration) almost disappear. This is because the C=O are reduced by H_2. Besides, Fig. 2b shows the typical XPS spectra of SnO_2 nanorods on reduced graphene sheets (SnO_2/rGss). The C1s spectra of sample were deconvoluted into three main peaks: C-C/C=C (284.5 eV), C-O (286.5 eV), and C=O (288.9 eV). These results indicating that SnO_2/graphene interface may be combined with C-O, which suggests a good adhesion of this SnO_2 nanorod within the present heterostructures (SnO_2/rGss).

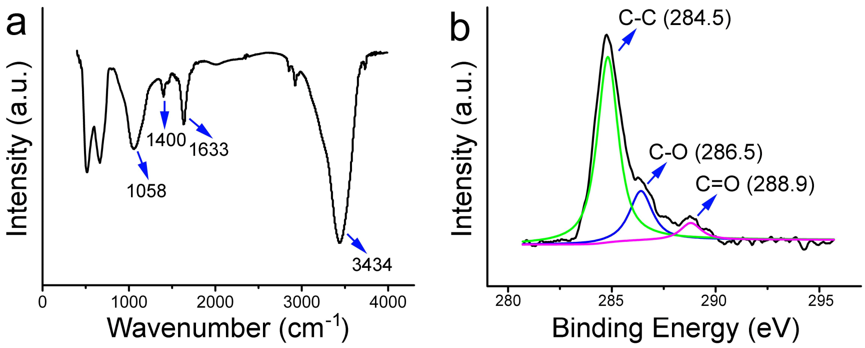

Fig. 4 (a) FTIR spectra of SnO_2 nanorods on reduced graphene sheets. (b) The XPS spectra for SnO_2 nanorods on reduced graphene sheets.

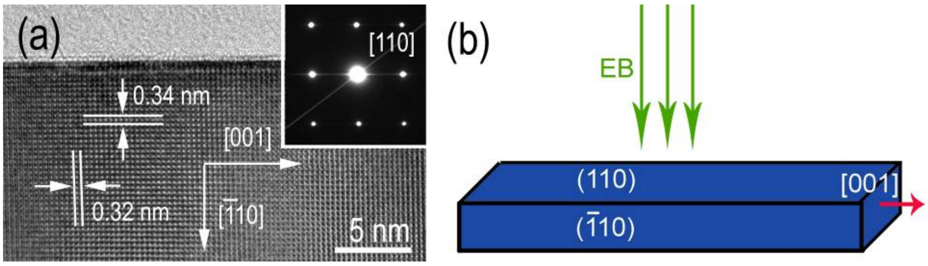

Fig. S5 (a) HRTEM image shows a SnO_2 nanorod, and an upper right inset depicts the ED pattern along the [001] zone axis of a tetragonal SnO_2 crystal. (b) Schematic diagram illustrates the geometrical morphology of the SnO_2 nanorod with respect to the e-beam orientation.

III. Controllable growth of SnO_2 nanorod arrays on a single side of free-standing rGss

For the present "NSDH" route, the influences of the concentration of $SnCl_4$ aqueous solution and hydrothermal reaction time on the growth of the heterostructures of SnO_2/rGs were then investigated. It was found that upon the same size and density of the SnO_2 nanocrystals seeded on the rGss, the concentration of $SnCl_4$ aqueous solution in the hydrothermal reaction had had an obvious effect on the diameter of the SnO_2 nanorods grown on the rGss. So, it is feasible to control the diameter of the SnO_2 nanorods on the rGss by simply tuning the concentration of an $SnCl_4$ aqueous solution. Different concentrations of 0.001, 0.005, 0.01, and 0.1 M of $SnCl_4$ for the aqueous solutions were tried, in which all the hydrothermal temperature and time were kept at 220 °C and 14 h, respectively, as shown by SEM images in Figs. S6 (a-d); obviously, the diameter of the SnO_2 nanorods on the rGss strongly increases with the concentration of $SnCl_4$ aqueous solution increasing, and is correspondingly estimated to be ~ 15, 25, 70, and 200 nm, respectively. Also, in our experiment, the samples with various hydrothermal growth times were prepared and investigated. Different hydrothermal growth times of 1, 6, and 12 h were examined, for all runs the hydrothermal temperature was kept at 220 °C, as shown by TEM images in Figs. S6 (e-g); the diameter and length of the SnO_2 nanorods grown on the rGss are correspondingly estimated to be ~ 5 nm and ~ 10 nm (Fig. S6e), ~ 15 nm and 110 nm (Fig. S6f), ~ 25 nm and 350 nm (Fig. S6g), respectively. Clearly, prolonging the hydrothermal growth time is beneficial for the growth of SnO_2 nanorods; for comparison, the effect of the hydrothermal growth time on the nanorods' length was more distinct than that for the nanorods' diameter. However, further extending the reaction time (e.g., 36 h, Fig. S6h) had no significant influences on the growth of the SnO_2 nanorods on the rGss.

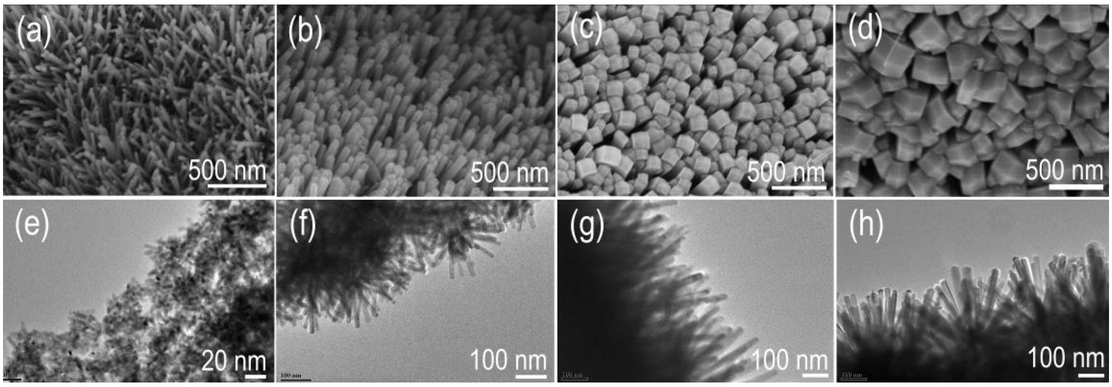

Fig. S6 SEM and TEM images demonstrate the as-grown heterostructures of SnO_2/rGss under different conditions: (a-d) the concentrations of $SnCl_4$ aqueous solution were of 0.001, 0.005, 0.01, and 0.1 M, respectively, for all runs the hydrothermal temperature and time were kept at 220 °C and 14 h, respectively, (e-h) the hydrothermal reaction time was of 1, 6, 12 and 36 h, respectively, for all tries the hydrothermal temperature was kept at 220 °C.

IV. Discussions on reliable evaluation of the strength values using the AFM-TEM holder

To quantitatively determine the adhering and breaking strength between the SnO_2 nanorods and the rGss, theAFM-TEM holder was used to perform direct tensile tests. To reliably evaluate the strength values, in the first instance, the electrical conversion factor (c) of the force sensor was calibrated. A silicon cantilever with a 30 nm thick layer of Pt-coating was fixed to a MEMS force sensor, whereas an Au wire was placed on the piezo-driven movable side of the holder. The X, Y, and Z positions of the cantilever and Au wire were adjusted with the nanoscale precision manipulations within the holder. The Si cantilever was tested against a bare Au wire (Fig. S7a) to obtain a force-displacement curve *(F-d)*. During the calibration, the *d* of the moving Au wire and the corresponding *F* (detected by the AFM sensor) were recorded, as shown in Fig. S7b. As seen from the *F-d* curve (with a noise level of ~ ±5 nN), this constant is related to the electrical sensitivity of the sensor and set to a value of ~ 1:5.2, on the basis of the *F-d* curve. So, in the present system, *c* is -5.2 mV nm^{-1}.

To reliably evaluate the adhesion strength between SnO_2 nanorods and the rGs during the *F-d* measurements, several factors should additionally be taken into account.

First, two stable and strong contacts between the top end of a given SnO_2 nanorod (grown on the rGs) and the AFM cantilever, and between the reverse side of the rGs' surface and the Au tip, respectively, are both required. To achieve these, we focused an e-beam onto the contact area of the rGs and Au tip, and the contact area of the SnO_2 nanorod top end and the AFM cantilever. This *in-situ* e-beam irradiation notably enhanced the adhesion forces (strength) due to a fact that a sort on nanowelding occurred around the two contact domains. Secondly, in order to exclude the influence of a contact angle, the Au tip was adjusted through the piezo-driven manipulations to get a perpendicular alignment between the cantilever and the SnO_2 nanorod by drifting the piezotube. Thirdly, SEM image reveals that areas of the two-layered heterostructures of SnO_2/rGss can be up to ~ 10-300 μm^2. We easily focused an e-beam onto the reverse side of the rGs' surface and Au tip to avoid e-beam irradiation breaking testing interface between SnO_2 and graphene sheet, as shown in Fig. S7c. So, we can easily achieve strong contacts between the reverse side of the rGs' surface and the Au tip to avoid breaking interface between SnO_2 and graphene sheet. Finally, though the tensile test was performed under irradiation of 200 kV electrons in the TEM, the increasing noise associated with that irradiation was rather small. due to using a low illumination intensity regime.

So, it is believed that the e-beam irradiation does not have an obvious influence on the evaluation of the strength values during the *F*-*d* measurements.

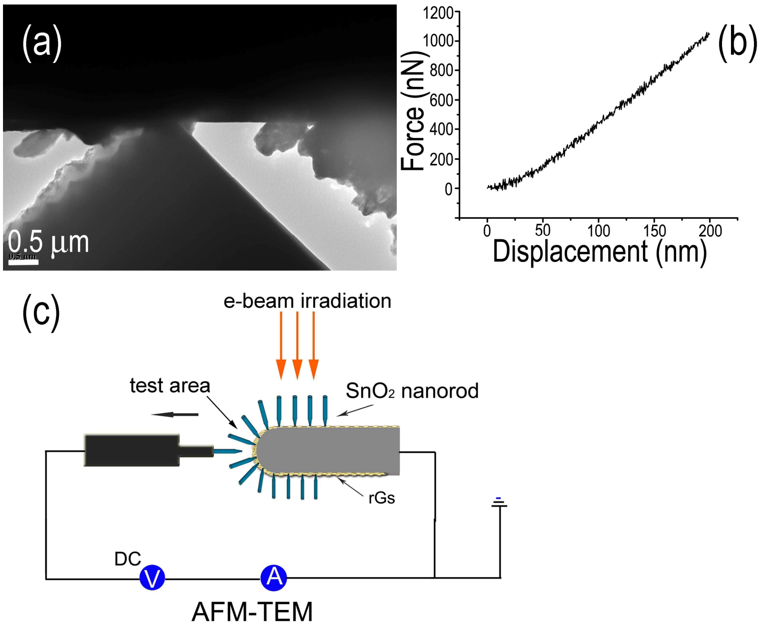

Fig. S7 (a) The Si cantilever against the bare Au wire. (b) Calibration plot of the electrical conversion factor. (c) Schematics setup illustrating e-beam irradiation on the rGs within the AFM-TEM holder.

V. Discussions on reliable evaluation of electrical behavior using the STM-TEM holder

In order to obtain accurate data with respect to the electrical properties, some factors, such as contact force, contamination atomic layers or even contact angle, should be carefully considered. First, an Au probe attached with the as-grown SnO_2/rGs heterostructures' sample was fixed to the holder frame, whereas a Pt tip was placed on its piezo-driven movable side. At the beginning, the relative positions of the tip and the probe were manually adjusted with tweezers under an optical microscope to get a minimal possible gap between them. Then, the X, Y, and Z positions of the Pt tip were adjusted through the piezo-driven manipulations with a nanoscale precision, and then the Pt tip approached a given SnO_2 nanorod on the rGs (adhered on the Au probe). With the Pt tip gradually approaching, a SnO_2 nanorod bridge was built between the Au probe and the Pt tip. Electron-induced deposition of an amorphous carbon was made around the contact domains between the SnO_2 nanorod and the Pt tip, and between the reverse side of the rGs' surface and the Au probe, to make sure that the SnO_2 nanorod was firmly bridged between them. Then, a current was applied to weld the SnO_2 nanorod to the Pt tip and to the Au probe (in fact, on the graphene sheet), respectively, so as to make two firm contacts between the SnO_2 nanorod and the Pt tip, and between the rGs and the Au probe. Due to a high resistance of the contact points, a high temperature was generated locally when the current flowed through the SnO_2 nanorod bridge based circuit. Thus new nanowelding took place around the SnO_2 nanorod's contact domains close to the Pt tip (electrode) and the Au probe (electrode), forming excellent low-resistant contacts between the SnO_2 nanorod and the two electrodes. The effects originated from the contact force and contamination atomic layers (on the electrodes) on electrical properties were thus minimized. In addition, in order to exclude the influence of an improper contact angle, the Pt tip was carefully adjusted through the piezo-driven manipulations with a nanoscale precision to make a nearly ideal perpendicular alignment between the Pt tip and the SnO_2 nanorod.

VI. Discussions about the electrical behavior of a SnO_2 nanorod (on the rGs) bridged between the Au probe and the Pt tip

It should be pointed that the electrical behavior of a system composed of SnO_2 nanorod grown on the rGs is not fully Ohmic across the entire bias interval from - 5 to 5 V. This is basically due to the two facts. First, despite excellent physical adhesion between the SnO_2 nanorod and the Pt tip, not perfect electrical contact may exist due to the presence of a thin layer of contaminating amorphous carbon coating on the Pt electrode. In our experiments, the consecutive *I-V* acquisitions were tried to overcome a high contact resistance by forcing the current to flow until an electric breakdown of the weak conducting layer took place. Secondly, although the SnO_2 nanorods are single crystals, their ends do not display flat surfaces, which may lead to a difficulty in making a perfect intimate contact between them and the electrodes. These structural and morphological factors may somehow influence the alignment of the Pt-SnO_2 Fermi surfaces. As a result, the electrical behavior of the SnO_2 nanorod based circuits is not fully linear across the entire bias interval.

VII. Field emission properties of the SnO_2/rGs heterostructures' cathodes as revealed using the TEM-STM holder

A parallel diode-type configuration for the *in situ* field emission (FE) measurements was developed by using a STM-TEM holder, which was arranged within a 200 kV TEM. A sample of the SnO_2/rGs heterostructures was ultrasonically dispersed in 10 mL of absolute ethanol to generate a homogeneous solution in a capped bottle, and then the solution was dripped onto a 200-mesh Cu TEM grid, which was dried in vacuum at 120 °C for 26 h to make the SnO_2/rGs heterostructures and to closely adhere them to the carbon film of a Cu mesh. The edge of the Cu mesh was fixed on a short Au rod with a diameter of 35 μm and then was cut into halves (perpendicular to Au rod axis) to make it flat for the FE measurement, as shown in Figs. S8a and 8b. We then folded the forepart of the Cu mesh where a piece of the SnO_2/rGs heterostructures was stuck, forming an angle (about 70°) between the folded part and the horizontal part, as shown in Figs. S8c and 8d. Then, the short Au rod fixed by the Cu mesh with the SnO_2/rGs heterostructures was attached to a fixed electrical sensor, whereas a Pt cantilever was placed on the piezo-driven movable side of the holder. A relative position between the Pt cantilever and the Cu mesh (or the short Au rod) was manually adjusted with tweezers under the optical microscope in order to obtain the possible minimal gap between them, which can be distinguished by eyes. Then, the X, Y, and Z positions of the Pt cantilever were adjusted through the nanoscale precision piezo-driven manipulations, to get a constant gap of ~ 10 μm between the Cu mesh and the Pt cantilever and to keep horizontal direction between the Cu mesh (with the SnO_2/rGs heterostructures stuck) and the Pt cantilever, as shown in Figs. S8e and 8f. Finally, on the basis of the model adopted from the classical FE, the FE properties of the present cathodes made of SnO_2/rGs heterostructures were evaluated, as shown in Fig. S8g.

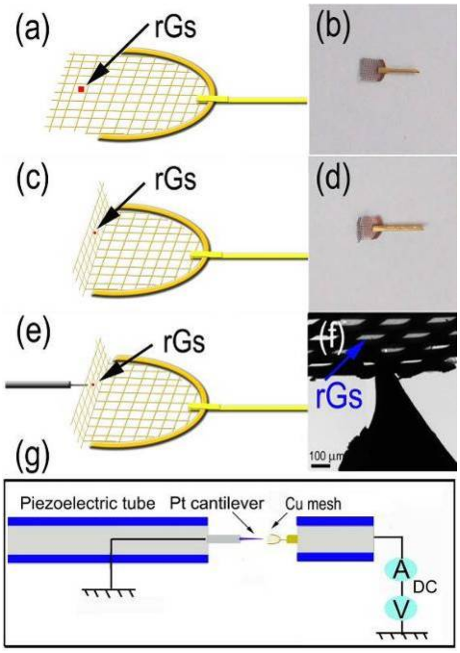

Fig. S8 Schematic illustrates the preparation of a setup for the measurement of FE from the SnO_2/rGs heterostructures' cathodes within the TEM-STM holder.

VIII. Detailed descriptions of the field emission theory

The field emission *I-V* curves are often analyzed using the Fowler-Nordheim (*F-N*) equation, a standard form of the *F-N* equation is

$$J = (a/\phi t(y)^2)F^2\exp(-b\phi^{3/2}\upsilon(y)/F) \qquad (1)$$

where J (A/m^2) is the current density, a and b are universal constants given by a = 1.541434×10^{-6} A eV V^{-2}, b = 6.830888×10^9 eV$^{-3/2}$ V m^{-1}, respectively, ϕ is the work function of the electron emitter, F (V/m) is the local field ($y = cF^{1/2}/\phi$, c = 3.794687×10^{-5} eV$^{-1/2}$ V m$^{1/2}$), and $t(y)$ and $\upsilon(y)$ are two functions of y, which can be approximated by $t(y)^2 = 1.1$ and $\upsilon(y) = 0.95 - y$. Assuming $I = JA$, with A (m^2) of the emission area, substitution of these expressions into Eq. (1) gives

$$I = 1.4\times10^{-6}AF^2/\phi\exp(9.84/\phi^{1/2})\exp(-6.49\times10^9\phi^{3/2}/F) \qquad (2)$$

Then, it can be written as

$$I \approx AF^2/\phi\exp(9.84/\phi^{1/2})\exp(-6.49\times10^9\phi^{3/2}/F) \qquad (3)$$

where A is a constant and ϕ is the work function. The local electric field F is related to the applied voltage V via $F = \beta V$, β, the field conversion factor. *F-N* plots may be obtained from *I-V* curves via plotting ln(I/V^2) vs 1/V, and from the slope S of the *F-N* plot, we can obtain $\beta = \frac{0.95B\phi^{3/2}d}{S}$. The *F-N* plots can be fitted very well by straight lines, indicating that the field emission of as-fabricated field emitter basically follows the *F-N* theory.

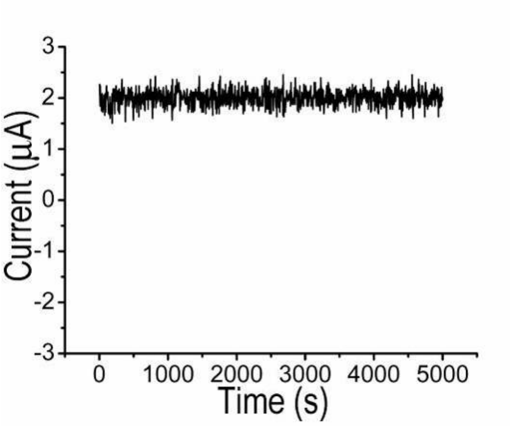

Fig. S9 The noise of the emission current at the initial state.

References

1 W. Z. Li, S. S. Xie, L. X. Qian, B. H. Chang, B. S. Zou, W. Y. Zhou, R. A. Zhao and G. Wang, *Science***,** 1996, **274**, 1701.

2 M. Terrones, N. Grobert, J. Olivares, J. P. Zhang, H. Terrones, K. Kordatos, W. K. Hsu, J. P. Hare, P. D. Townsend, K. Prassides and A. K. Cheetham, H. W. Kroto and D. R. M. Walton, *Nature*, 1997, **388**, 52.

3 X. M. Feng, R. M. Li, Y. W. Ma, R. F. Chen, N. E. Shi, Q. L. Fan and W. Huang, *Adv. Funct. Mater.*, 2011, **21**, 2989.

4 P. G. Ren, D. X. Yan, X. Ji, T. Chen and Z. M. Li, *Nanotechnology*, 2011, **22**, 055705.

5 S. Park , J. An, I. Jung, R. D. Piner, S. J. An, X. Li, A. Velamakanni and R. S. Ruoff, *Nano Lett.*, 2009, **9**, 1593.

6 D. Li, M. B. Muller, S. Gilje, R. B. Kaner and G. G. Wallace, *Nat. Nanotechnol.,* 2008, **3**, 101.